Simulation of hysteresis in magnetic nanoparticles with Nosé thermostating

Daniel T. Robb,* Linda E. Reichl, and Eshel Faraggi
Center for Studies in Statistical Mechanics and Complex Systems, The University of Texas at Austin, Austin, Texas 78712
(Received 17 March 2002; revised manuscript received 6 March 2003; published 28 May 2003)

The magnetic hysteresis of a two-dimensional lattice of rotors with four-way anisotropy interaction and a Heisenberg exchange interaction is studied. The Hamiltonian dynamics of the lattice is thermostated using the Nosé thermostat, resulting in a system that approaches thermal equilibrium and which under certain conditions can remain in metastable states. Using physically realistic values for the interactions in a nanoparticle of monolayer thickness, we locate the Curie temperature of our lattice by determining the peak of the heat capacity curve. We then compare the coercive field of our two-dimensional lattice below this Curie temperature to the coercive field of an elliptical cobalt nanoparticle measured in experiment. We find an order of magnitude agreement between our lattice model and the experimental results, even though the value of the anisotropy used is more appropriate for a monolayer film than for the nanoparticle.

DOI: 10.1103/PhysRevE.67.056130 PACS number(s): 05.10.−a, 75.60.Ej, 75.50.Tt, 05.45.Jn

I. INTRODUCTION

Over the past several decades, most of the dynamical studies of hysteresis in magnetic systems have involved the use of Monte Carlo techniques [1–3] to reproduce hysteretic behavior. However, Rapaport and Landau [4] have shown that it is possible to reproduce the critical dynamics of a classical Heisenberg spin model by using a Gaussian thermostat applied directly to the Newtonian dynamics of a system of classical Heisenberg rotors (the rotor model will be explained in Sec. II).

In this paper, we will extend the approach of Rapaport and Landau to the study of hysteresis in a periodic lattice of rotors. However, instead of using a Gaussian thermostat, we will use a Nosé thermostat. While the Gaussian thermostat is quite useful, the Nosé thermostat gives a slightly more accurate thermal distribution, and deserves investigation because of its basis in the Hamiltonian dynamics. The rotors each have a moment of inertia and a three-component magnetic moment, and so have a kinetic energy as well as a potential energy, and the possibility for an out-of-plane magnetization. The rotors interact via a Heisenberg exchange interaction as well as the K_4 anisotropy term used by Moschel *et al.* to study the roughness in thin magnetic films [5].

In Sec. II, we introduce the dynamics of the lattice of rotors and show that the phase space is largely chaotic by computing Lyapounov exponents for a group of random initial conditions. We also compute the density of states and the expected canonical distribution for the system. In Sec. III, we apply thermostating to the Hamiltonian equations of motion for the lattice using techniques introduced by Nosé, and compare the thermal distributions obtained with the Nosé thermostat to the expected canonical distributions. In Sec. IV, we use the thermostated equations to determine the dependence of the internal energy and the heat capacity on temperature, enabling us to locate the critical point of the lattice. In Sec. V, we show that our dynamical system produces hysteresis when a changing magnetic field is applied, and compare our results to experimental data obtained by Wernsdorfer *et al.* [6] for elliptical cobalt nanoparticles with similar size. We obtain an order of magnitude agreement, and give suggestions for changes to the model which may improve the agreement. In Sec. VI, we compare the reversal of magnetization in our rotor model to the reversal of magnetization in the cobalt nanoparticle, and by examining the decay times are able to set a time scale for our model. Finally, in Sec. VII, we make some concluding remarks.

II. SPIN DYNAMICS ON A SURFACE

The dynamics of the lattice is determined by the exchange interaction and the surface anisotropy interaction of the thin film it represents, as well as by the interaction with the applied magnetic field. Each rotor consists of a spherical mass distribution with moment of inertia I (the moment of inertia tensor is diagonal with entries equal to I) and a magnetic moment vector that is fixed along the body z axis of the rotor. We represent the three-component magnetic moment vector of the ith rotor as $\vec{\mu}_i = \mu \hat{\vec{n}}_i$, where μ is the magnitude of the magnetic moment and the unit vector $\hat{\vec{n}}_i = (n_{ix}, n_{iy}, n_{iz})$ gives its direction in the lab frame.

The spherical rotor with attached magnetic moment, introduced by Rapaport and Landau [4], should not be viewed as a literal model of an atom in the thin film lattice, since the magnetic moments in an actual thin film rotate without an accompanying rotation of the atoms. The kinetic energy of the rotors is best seen as representing the thermal degrees of freedom of the thin film (involving energy states within the atoms, lattice vibrations, etc.), which act as a heat bath for the magnetic moments. The rotors then allow us to use the technique of Nosé thermostatting to introduce thermal effects. In addition, following the work of Moschel *et al.* [5] in modeling hysteresis in thin films, we take each rotor to represent a $b \times b$ block of aligned atomic spins. This ''spin blocking'' allows us to model larger samples with our available computing power. Since the exchange length in cobalt is about 7.0 nm [7] and the lattice spacing is 0.355 nm [8], we can choose a value of $b = 20$ for spin blocking.

*Email address: drobb@alumni.utexas.net

TABLE I. The largest Lyapounov exponents for ten initial conditions of the lattice of rotors for an average of the three cases $(d,\Delta t)$, $(d/2,\Delta t)$, and $(d,\Delta t/2)$; the first row shows data with all three interactions present, while the second row shows data with just the exchange interaction.

Initial condition	1	2	3	4	5	6	7	8	9	10
All interactions	0.643	0.663	0.649	0.645	0.667	0.662	0.675	0.676	0.651	0.658
Just exchange	0.492	0.507	0.491	0.503	0.516	0.489	0.511	0.516	0.493	0.483

The Lagrangian for the lattice in the laboratory frame can be written as

$$L=\frac{1}{2}I\sum_{i=1}^{N}\omega_i^2+J\sum_{\langle i,j\rangle}\hat{\vec{n}}_i\cdot\hat{\vec{n}}_j+\mu\mathcal{H}(t)b^2\sum_{i=1}^{N}n_{ix}+\sum_{i=1}^{N}K_4a^2b^2\frac{(n_{ix}^2-n_{iy}^2)^2}{(n_{ix}^2+n_{iy}^2)^{1.5}},\tag{1}$$

where $\vec{\omega}_i$ is the angular velocity of the ith rotor, I is the moment of inertia of each rotor, J is the strength of the Heisenberg exchange coupling, K_4 is the strength of the surface anisotropy interaction, a is the lattice spacing, and $\mathcal{H}(t)=\mathcal{H}_0\cos(2\pi ft)$ is the external magnetic field, with magnitude $\mathcal{H}_0$ and frequency f. The fact that we are dealing with blocks of spins introduces a factor of b^2 in the magnetic field interaction and the K_4 interaction. As pointed out by Moschel *et al.* [5], the spin blocking leaves the exchange interaction unchanged [9], producing a Curie temperature independent of the size of the spin blocks, as one would expect physically. The label $\langle i,j\rangle$, in the summation means that we sum over each pair of the nearest neighbors (nn) just once.

We can use Euler angles to describe the dynamics of this system in the lab frame (fixed inertial frame). If we label the three axes of the fixed inertial frame x, y, z, and the corresponding axes of the body-fixed frame as 1,2,3, then the Euler angles are defined as follows: ϕ is the angle of rotation of the 1-axis about the z axis; θ is the angle of rotation of the 3-axis about the new 1-axis; and ψ is the angle of rotation of the 1-axis about the new 3-axis [10]. The components of the unit vector $\hat{\vec{n}}_i$ (which lies along the body frame 3-axis) with respect to the lab frame axes are

$$n_{ix}=\sin\theta_i\,\sin\phi_i,\quad n_{iy}=-\sin\theta_i\,\cos\phi_i,\quad n_{iz}=\cos\theta_i.\tag{2}$$

We can now write the Lagrangian in terms of Euler angles as

$$L=\frac{1}{2}I\sum_{i=1}^{N}\left[\dot{\phi}_i^2+\dot{\theta}_i^2+\dot{\psi}_i^2+2\dot{\phi}_i\dot{\psi}_i\cos(\theta_i)\right]-U(\theta_i,\phi_i,t),\tag{3}$$

where $\dot{\phi}_i=d\phi_i/dt$, $\dot{\theta}_i=d\theta_i/dt$, and $\dot{\psi}_i=d\psi_i/dt$, and the potential energy is given by

$$\begin{aligned}U(\theta_i,\phi_i,t)=&-J\sum_{\langle i,j\rangle}\left[\sin(\theta_i)\sin(\theta_j)\cos(\phi_i-\phi_j)+\cos(\theta_i)\cos(\theta_j)\right]\\&-\mu\mathcal{H}(t)b^2\sum_{i=1}^{N}\left[\sin(\theta_i)\sin(\phi_i)\right]\\&-K_4a^2b^2\sum_{i=1}^{N}\left[\cos^2(2\phi_i)\sin(\theta_i)\right].\end{aligned}\tag{4}$$

The Hamiltonian H then takes the form

$$H=\frac{1}{2I}\sum_{i=1}^{N}\left[p_{\theta,i}^2+\frac{[p_{\phi,i}-p_{\psi,i}\cos(\theta_i)]^2}{\sin^2(\theta_i)}+p_{\psi,i}^2\right]+U(\theta_i,\phi_i,t),\tag{5}$$

where $p_{\theta,i}$, $p_{\phi,i}$, and $p_{\psi,i}$ are the canonical momenta of the rotors.

It is useful to write the Hamiltonian in dimensionless units. If we measure all energies in units of the exchange coupling energy J, we can introduce a dimensionless time $t'=\sqrt{J/I}t$, frequency $f'=\sqrt{I/J}f$, magnetic energy $h=\mu\mathcal{H}_0b^2/J$, anisotropy energy $\kappa_4=K_4a^2b^2/J$, angular velocity $\dot{\phi}_i'=\sqrt{I/J}\dot{\phi}_i$, angular momentum $p'_{\phi,i}=p_{\phi,i}/\sqrt{IJ}$, and Hamiltonian $H'=H/J$. If we substitute these quantities into Eq. (5), and then drop the primes, we obtain

$$H=\frac{1}{2}\sum_{i=1}^{N}\left[p_{\theta,i}^2+\frac{[p_{\phi,i}-p_{\psi,i}\cos(\theta_i)]^2}{\sin^2(\theta_i)}+p_{\psi,i}^2\right]+V(\theta_i,\phi_i,t),\tag{6}$$

where

$$\begin{aligned}V(\theta_i,\phi_i,t)=&-\sum_{\langle i,j\rangle}\left[\sin(\theta_i)\sin(\theta_j)\cos(\phi_i-\phi_j)+\cos(\theta_i)\cos(\theta_j)\right]-h(t)\sum_{i=1}^{N}\left[\sin(\theta_i)\sin(\phi_i)\right]\\&-\kappa_4\sum_{i=1}^{N}\left[\cos^2(2\phi_i)\sin(\theta_i)\right]\end{aligned}\tag{7}$$

and $h(t)=h_0\cos(2\pi ft)$. The equations of motion derived from this dimensionless Hamiltonian are given by

$$\frac{d\theta_i}{dt} = p_{\theta,i}, \quad \frac{d\phi_i}{dt} = \frac{[p_{\phi,i} - p_{\psi,i}\cos(\theta_i)]}{\sin^2(\theta_i)},$$

$$\frac{d\psi_i}{dt} = p_{\psi,i} - \frac{[p_{\phi,i} - p_{\psi,i}\cos(\theta_i)]\cos(\theta_i)}{\sin^2(\theta_i)},$$

$$\frac{dp_{\theta,i}}{dt} = -\frac{\partial V}{\partial \theta_i} - \frac{[p_{\phi,i} - p_{\psi,i}\cos(\theta_i)][p_{\psi,i}\sin^2(\theta_i)] - [p_{\phi,i} - p_{\psi,i}\cos(\theta_i)]^2[\cos(\theta_i)]}{\sin^3(\theta_i)}, \tag{8}$$

$$\frac{dp_{\phi,i}}{dt} = -\frac{\partial V}{\partial \phi_i}, \quad \frac{dp_{\psi,i}}{dt} = -\frac{\partial V}{\partial \psi_i} = 0.$$

We perform subsequent computations using this dimensionless system of dynamical variables.

Since we will compare our results to the magnetic properties of small cobalt nanoparticles [6], we need to determine a value of the exchange coupling J in cobalt. Craik and Tebble [11] summarize a group of experiments done in the 1950s to determine the exchange constant, A, for cobalt in a continuum spin model with Heisenberg interaction. They report that methods of fitting the Curie temperature of cobalt, fitting the low temperature dependence of magnetization, and predicting results of spin-wave resonance experiments have given values of $A = 1.03\times10^{-6}$ erg/cm, 1.5×10^{-6} erg/cm, and 1.3×10^{-6} erg/cm. The exchange coupling, J, can be related to A by the expression $J = 2Aa/\nu$ [11], with a the lattice constant (0.355 nm in cobalt) and ν the number of atoms per unit cell of an fcc lattice (4), producing a range for $J = (1.8\text{–}2.5)\times10^{-21}$ J. We can choose $J = 2.0\times10^{-21}$ J as a convenient value.

We can estimate the parameter κ_4 from a paper by Kowalewski *et al.* [12] which gives the surface anisotropy of cobalt at 77 K as $K_4 = 1.86\times10^{-5}$ J/m^2. Because the experiment we will compare to is done at a low temperature, and the strength of the surface anisotropy increases at lower temperature [13], we will choose $K_4 = 2.65\times10^{-5}$ J/m^2 as a reasonable value. In units of the exchange coupling, this gives $\kappa_4 = K_4 a^2 b^2/J = 0.67$.

The magnetic field energy needed to produce reversal and give hysteresis in the model was found by trial and error, and will be presented and then compared with the field $\mathcal{H}$ needed to produce reversal in experiments. The temperatures for the model are expressed in units of J; for example, we will produce data for hysteresis loops at $T = 20.0$ K, $T = 60.0$ K, and $T = 100.0$ K, which correspond to $kT/J = 0.14$, 0.42 and 0.69, respectively. Finally, to determine a value for I, since the rotors are not a direct physical model but allow for the thermalization of the magnetic moments, we will compare the relaxation times of the model to experiment and choose a value of I that produces agreement with experimental results.

A. Lyapounov exponents for the lattice of rotors

In order for the Nosé technique to thermalize the lattice, we need a classical phase space that is largely chaotic, so the trajectories of the thermostated system can sample most of the available points in phase space. Posch, Hoover, and Vesely [14] found that a one-dimensional harmonic oscillator is not fully thermalized by the Nosé thermostat; slightly more complex systems, however, are thermalized. To estimate the degree of chaos in the lattice of rotors, in this section we calculate the largest Lyapounov exponents of the 10×10 lattice with the Hamiltonian, Eq. (6), and potential Eq. (7). We choose the value $\kappa_4 = 0.67$, as indicated above, and a constant magnetic field $h = h_{const} = 1.00$ in place of the time-varying field $h(t)$.

In finding the largest Lyapounov exponents, we use the algorithm due to Benettin [15] which records the degree of separation of nearby trajectories for a series of small time steps, rescaling to the initial separation at each step. A very useful summary of the method is given in Ref. [16]. For a small enough time step Δt and (generic) separation d, the exponent found is independent of the time step and the separation. We verified this independence for our calculations, and we also verified that energy is conserved for the base trajectory and the separation is rescaled to the initial value at each time step. Using an Adams-Gear integration routine, we integrated the dimensionless equations (8) for both the base and nearby trajectories to a maximum time $t = 400.0$. The ten initial conditions were chosen to be random in the configuration space of the potential energy, and to produce a kinetic energy consistent with a temperature $T = 133$ K.

The results for the Lyapounov exponents are shown in Table I. As mentioned above, to ensure that the time step and separation were chosen small enough, for each initial condition we also calculated the exponent for the case where the time step was halved, and for the case where the separation was (roughly) halved. For the three cases $(d,\Delta t)$, $(d/2,\Delta t)$, and $(d,\Delta t/2)$, the time step was $\Delta t = 5.0\times10^{-3}$ for all initial conditions, while the separation d had range $[3.1\times10^{-3}, 3.7\times10^{-3}]$ and the halved separation $d/2$ had range $[1.5\times10^{-3}, 1.9\times10^{-3}]$. In general, the three exponents (not shown in the table) agreed to two significant figures. The average of the three values was taken as a best estimate of the largest Lyapounov exponent for that initial condition, and is presented in the table. For each of the ten initial conditions, an average exponent well into the range associated with chaos was found. Although the size of the

phase space makes a systematic study of the degree of chaos impractical, the consistency of these ten Lyapounov exponents suggests that the phase space consists mainly of a large connected chaotic region.

In addition, we have calculated Lyapounov exponents for the lattice of rotors with just the exchange interaction. The results in Table I show that the exchange interaction alone is enough to produce chaos at least for ten randomly chosen points, so that the thermalization we expect for the system does not depend on the value of the field h or anisotropy κ_4 or other interactions which might be included. (An exception to this would be the introduction of a very strong magnetic field or other interaction, which could dominate the exchange interaction and potentially give a nearly integrable system). In general, however, when the exchange interaction is present, the phase space of the lattice is significantly chaotic, and we expect that the Nosé thermostat will thermalize the lattice to a large extent.

B. Finding the expected canonical distributions

We need to check that the thermalization induced by the Nosé thermostat is consistent with the canonical ensemble expected from thermodynamics. Since the kinetic energy depends only on $(\vec{\omega}_1, \ldots, \vec{\omega}_N)$ and the potential energy depends only on the magnetic moment orientations $(\hat{\vec{n}}_1, \ldots, \hat{\vec{n}}_N)$, the canonical distributions for the kinetic and potential energies separate. That is, the canonical distribution for the total energy, $P(H,T)$, is the product of the two distributions $P(K,T)$ and $P(V,T)$, where

$$P(K,T) = \frac{g_1(K)e^{-\beta K}}{\int_0^{K_{max}} g_1(K)e^{-\beta K}dK} \tag{9}$$

and

$$P(V,T) = \frac{g_2(V)e^{-\beta V}}{\int_{V_{min}}^{V_{max}} g_2(V)e^{-\beta V}dV}. \tag{10}$$

The quantities $g_1(K)$ and $g_2(V)$ are the kinetic energy and the potential energy density of states, respectively. If we can determine $g_1(K)$ and $g_2(V)$, then we can find the expected canonical distributions for the thermostated systems.

1. Kinetic energy density of states

We first find the density of states $g_1(K)$ for the total kinetic energy of the 10×10 lattice. We note that the kinetic energy of N rotors is given by

$$K = \frac{1}{2}\sum_{i=1}^{N} (\omega_i)^2 = \frac{1}{2}\Omega^2, \tag{11}$$

where $\vec{\Omega} = (\vec{\omega}_1, \ldots, \vec{\omega}_N)$.

To find $g_1(K)$, we can use a standard procedure (see, e.g., Ref. [17]) for finding the density of states in the case where the expression for the energy is quadratic in the phase space variables. We divide the volume in Ω space into small (and uniform) volume elements $\Delta\mathcal{V}$, each representing a different state of the angular velocities $(\vec{\omega}_1, \ldots, \vec{\omega}_N)$. The total number of these states with kinetic energy less than K is $N(K) = \mathcal{V}(K)/\Delta\mathcal{V}$, where $\mathcal{V}(K)$ is the volume of a hypersphere in $\vec{\Omega}$ space whose surface has kinetic energy K.

From Eq. (11), $\mathcal{V}(K)$ is also the volume of a sphere with radius $|\vec{\Omega}| = \sqrt{2K}$. Since each of the N rotors has three degrees of freedom for the 10×10 lattice, the $\vec{\Omega}$ space has $3N$ dimensions. Using the fact that a $3N$ dimensional sphere has a volume $\mathcal{V}(r) = C_1 r^{3N}$ (with C_1 a geometrical factor), this gives

$$N(K) = \frac{C_1(2^{3N/2})K^{3N/2}}{\Delta\mathcal{V}}. \tag{12}$$

Since the kinetic energy has no upper limit, we need to set a maximum kinetic energy to arrive at a normalized density of states. Since we will use temperatures below $k_BT = 5.0J$ (725 K), we set a maximum kinetic energy $K_{max} \approx 3\times\frac{3}{2}Nk_BT$ to ensure that the canonical distribution we calculate will include all the kinetic energies the thermostated system will encounter. (Note that as long as K_{max} is set safely above the energy range of the canonical distribution, the exact value of K_{max} will not affect the canonical distribution calculated.) The fraction of allowed states with kinetic energy less than K is then

$$P(K) = \frac{N(K)}{N(K_{max})} = \frac{(K)^{3N/2}}{(K_{max})^{3N/2}}. \tag{13}$$

We can take the derivative to find the density of states, giving

$$g_1(K) = \frac{dP}{dK} = \left(\frac{3N}{2}\right)\frac{(K)^{3N/2-1}}{(K_{max})^{3N/2}}. \tag{14}$$

For a 10×10 lattice, this gives $g_1(K) = 150K^{149}/K_{max}^{150}$, with $K_{max} = 2000.0$ a convenient maximum value.

2. Potential energy density of states

For a 10×10 lattice, the potential energy, Eq. (7), depends in a complex way on the angles (θ_i, ϕ_i) for $i = 1, \ldots, 100$, and in many cases several values of the 200 angles will produce the same potential energy. We cannot find an analytic expression for $g_2(V)$, and need to calculate it numerically. Since the 10×10 lattice has a very large phase space, it is not practical to place a finely spaced grid on the phase space and calculate energies at the points of the grid. Instead, we sample the large phase space by choosing a large number of random points at which to calculate the energy. If we sample a large number of points (here 10^7 points), and then sort the energies found into a histogram with fairly few bins, then the sampled probability in each bin approximates the actual probability very closely. Since the probability $g_2(V)dV$ represents a fraction of the phase space volume, if we choose values of θ_i and ϕ_i with uniform probability in the ranges $[0,\pi]$ and $[0,2\pi]$, we need to weight the contri-

bution of each energy found by the volume element $\Pi_{i=1}^{N} \sin(\theta_i)\Delta\theta_i\Delta\phi_i$, and then normalize the resulting distribution.

Sampling N points from the phase space, each with a probability p_j of having an energy in the jth bin, we expect the average number of points falling in the jth bin to be Np_j. The standard deviation of the distribution of the actual number of points in the bin is given by $\Delta(Np_j)$, and it can be shown that the relative width $\Delta(Np_j)/Np_j$, which is a measure of the accuracy of the sampling method for that bin, increases as the probability p_j decreases. In our case, sampling 10^7 points from the phase space, we find that the relative width is 10% for a bin with probability 10^{-5}, and 35% for a bin with probability 10^{-6}. In performing this calculation for the 10×10 lattice, we found that the probability of bins in the energy histogram dropped below $p=10^{-5}$ for energies below $E=-85.0$, and thus the density of states is only reliable down to this energy. For temperatures below $kT=4.0$, energies below $E=-85.0$ begin to have an appreciable probability in the canonical distribution, so for the 10×10 lattice we can only reliably calculate the thermal distribution for $kT\geqslant4.0$.

If we consider smaller lattices, however, we can find more accurate thermal distributions for lower temperatures. In order to give an evidence that the Nosé thermostat does give nearly a thermal distribution for the 10×10 lattice, we will calculate potential energy densities of states for the 2×2, 4×4, and 6×6 lattices and argue that the trends we see will continue with increasing lattice size. We present the densities of states for the 2×2, 4×4 and 6×6 lattices in Fig. 1. As described above, the calculation was made by choosing 10^7 points at random from the configuration (potential energy) part of the phase space, and then including the relative volume of each point found in the appropriate bin of an energy histogram. The requirement that the probability be larger than 10^{-5} to give better than 10% accuracy makes the densities of states found accurate in the energy ranges $[-9.85,4.0]$, $[-27.0,15.0]$, $[-40.0,14.0]$ for the 2×2, 4×4, and 6×6 lattices, respectively.

We will use the densities of states found here, and the resulting expressions for the canonical distributions, Eqs. (9) and (10), to show that the 10×10 lattice is well thermalized by the Nosé thermostat. In the section following, we derive the thermostated equation of motion for the 10×10 rotor lattice, and then compare the canonical distributions obtained from the thermostated equations to those obtained above. We will find good agreement.

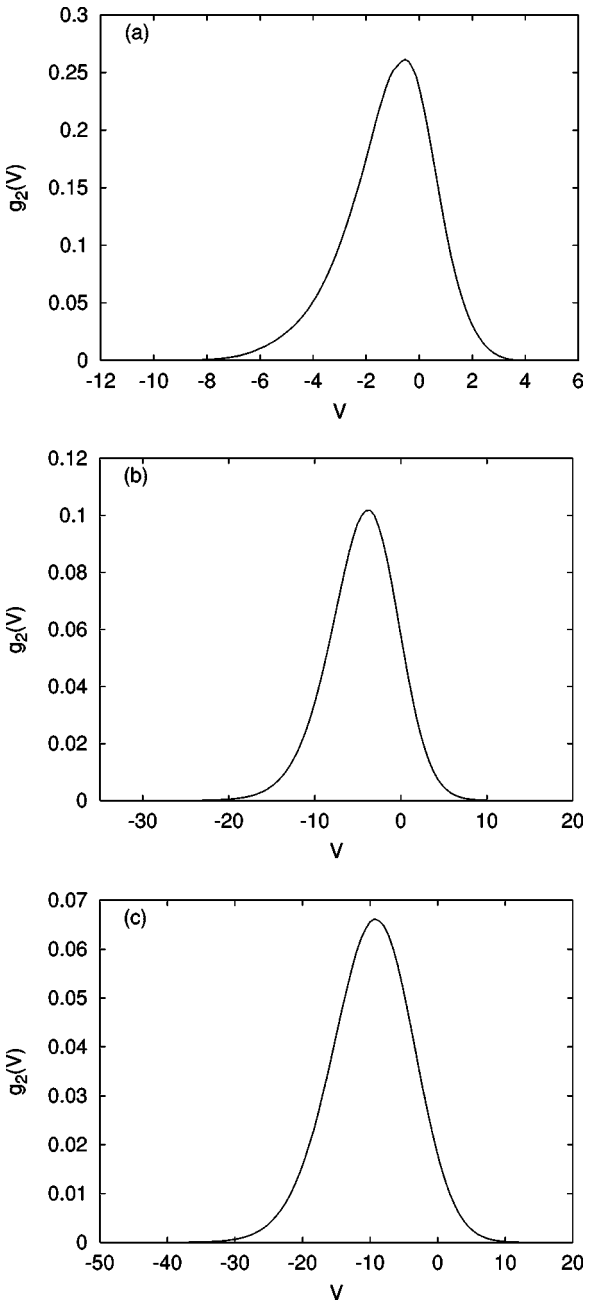

FIG. 1. Potential energy density of states, $g_2(V)$, for $\kappa_4=0.67$ and $h=h_{const}=1.00$. Both V and $g_2(V)$ are plotted in the dimensionless units defined in Sec. II. (a) 2×2 lattice, (b) 4×4 lattice, and (c) 6×6 lattice.

III. THE NOSÉ THERMOSTAT

Let us now return to the equations of motion and include a thermostat that will build temperature fluctuations and dissipation into the equations of motion. We will use the thermostatting procedure first introduced by Nosé in 1984 [18], a very ingenious method for generating a canonical distribution of energies from molecular dynamics equations. In this method, an extra ''Nosé'' degree of freedom (dof) is added to a Hamiltonian system; the Nosé dof couples to the kinetic energy of the original system, and together with the original dof's forms an extended Hamiltonian system. If the thermostated system is ergodic in the extended phase space (which requires that the unthermostated phase space be sufficiently chaotic), it can be shown that the energies visited by the Nosé thermostated system follow a canonical distribution for both the kinetic and potential energies [19].

A. Equations of motion with Nosé thermostat

The Nosé thermostatting procedure is based on an ''extended'' Lagrangian that can be written as

$$L_{ext}=\frac{1}{2}\sum_{i=1}^{N} S^2[\dot{\Phi}_i^2+\dot{\Theta}_i^2+\dot{\Psi}_i^2+2\dot{\Phi}_i\dot{\Psi}_i\cos(\Theta_i)]$$

$$-V(\Theta_i,\Phi_i,\tau)+\frac{Q\dot{S}^2}{2}-3Nk_BT\ln(S). \tag{15}$$

where the thermal energy k_BT is measured in units of the exchange coupling, J, $\dot{\Phi}_i=d\Phi_i/d\tau$, $\dot{\Theta}_i=d\Theta_i/d\tau$, $\dot{\Psi}_i=d\Psi_i/d\tau$, $\dot{S}_i=dS_i/d\tau$, τ is the dimensionless time in the extended dynamical system, and

$$V(\Theta_i,\Phi_i,\tau)=-\sum_{\langle i,j\rangle}[\sin(\Theta_i)\sin(\Theta_j)\cos(\Phi_i-\Phi_j)+\cos(\Theta_i)\cos(\Theta_j)]$$
$$-h(\tau)\sum_{i=1}^{N}[\sin(\Theta_i)\sin(\Phi_i)]$$
$$-\kappa_4\sum_{i=1}^{N}[\cos^2(2\Phi_i)\sin(\Theta_i)]. \tag{16}$$

The quantity Q is a dimensionless weighting factor that controls the rate at that fluctuations occur and S is an additional dimensionless degree of freedom which acts as an effective heat bath. The factor $3N$ is the total number of degrees of freedom of the lattice of rotors. The equations of motion in the extended dynamical system are given by the Euler-Lagrange equations

$$\frac{d}{d\tau}\left(\frac{\partial L_{ext}}{\partial\dot{A}_{k,i}}\right)=\left(\frac{\partial L_{ext}}{\partial A_{k,i}}\right), \tag{17}$$

where $k=1,2,3,4$, $A_{1,i}=\Phi_i$, $A_{2,i}=\Theta_i$, $A_{3,i}=\Psi_i$, and $A_{4,i}=S$.

The relation between the *virtual* variables that appear in the extended Lagrangian L_{ext} and the physical variables that appear in Eq. (3) is as follows. Since the squared quantities in the kinetic energy term of a Lagrangian are by definition the physical velocities, the positions and velocities in the physical system and the extended system are related by

$$\phi_i=\Phi_i,\quad \theta_i=\Theta_i,\quad \psi_i=\Psi_i,\quad \frac{d\phi_i}{dt}=S\frac{d\Phi_i}{d\tau},$$

$$\frac{d\theta_i}{dt}=S\frac{d\Theta_i}{d\tau},\quad \frac{d\psi_i}{dt}=S\frac{d\Psi_i}{d\tau}. \tag{18}$$

This implies that the (dimensionless) physical time t and the time τ in the extended system satisfy the condition

$$t=\int^{\tau}\frac{d\tau'}{S},\quad dt=\frac{d\tau}{S}, \tag{19}$$

so that the times in the physical system and the extended system evolve at different rates.

The Hamiltonian for the extended system can be written as

$$H_{ext}=\frac{1}{2S^2}\sum_{i=1}^{N}\left(P_{\Theta,i}^2+\frac{[P_{\Phi,i}-\cos(\Theta_i)P_{\Psi,i}]^2}{\sin^2(\Theta_i)}+P_{\Psi,i}^2\right)$$
$$+V(\Theta_i,\Phi_i,\tau)+\frac{P_S^2}{2Q}+3Nk_BT\ln(S). \tag{20}$$

The equations of motion that result from this extended Hamiltonian are given by

$$\frac{dP_{\Theta,i}}{d\tau}=-\frac{\partial V}{\partial\Theta_i}-\frac{[P_{\Theta,i}-\cos(\Theta_i)P_{\Psi,i}]P_{\Psi,i}}{S^2\sin(\Theta_i)}+\frac{[P_{\Phi,i}-\cos(\Theta_i)P_{\Psi,i}]^2\cos(\Theta_i)}{S^2\sin^3(\Theta_i)},$$

$$\frac{dP_{\Phi,i}}{d\tau}=-\frac{\partial V}{\partial\Phi_i},\quad \frac{dP_{\Psi,i}}{d\tau}=0,$$

$$\frac{dP_S}{d\tau}=\frac{1}{S^3}\sum_{i=1}^{N}\left(P_{\Theta,i}^2+\frac{[P_{\Phi,i}-\cos(\Theta_i)P_{\Psi,i}]^2}{\sin^2(\Theta_i)}+P_{\Psi,i}^2\right)-\frac{3Nk_BT}{S}, \tag{21}$$

$$\frac{d\Theta_i}{d\tau}=\frac{P_{\Theta,i}}{S^2},\quad \frac{d\Phi_i}{d\tau}=\frac{[P_{\Phi,i}-\cos(\Theta_i)P_{\Psi,i}]}{S^2\sin^2(\Theta_i)},$$

$$\frac{d\Psi_i}{d\tau}=\frac{P_{\Psi,i}}{S^2}-\frac{[P_{\Phi,i}-\cos(\Theta_i)P_{\Psi,i}]\cos(\Theta_i)}{S^2\sin^2(\Theta_i)},\quad \frac{dS}{d\tau}=\frac{P_S}{Q}.$$

The physical angular momenta are related to the angular momenta in the extended dynamical system as

$$p_\phi=\frac{P_\Phi}{S},\quad p_\theta=\frac{P_\Theta}{S},\quad p_\psi=\frac{P_\Psi}{S}. \tag{22}$$

For the extended dynamical system, the equations of motion for the variables $P_{\Phi,i}$, $P_{\Theta,i}$, $P_{\Psi,i}$, P_S, Φ_i, Θ_i, Ψ_i, S are obtained from the Hamiltonian, Eq. (20) using Hamilton's equations. However, the equations of motion for the physical variables, $p_{\phi,i}$, $p_{\theta,i}$, $p_{\psi,i}$, ϕ_i, θ_i, ψ_i in the thermostated system cannot be obtained from a Hamiltonian. The Nosé thermostating causes the energy of the physical degrees of freedom (that is, excluding the extra Nosé degree of freedom) to explore a canonical distribution at temperature T. The equations of motion for the physical variables $p_{\phi,i}$, $p_{\theta,i}$, $p_{\psi,i}$, ϕ_i, θ_i, ψ_i must be obtained directly from the equations of motion for the variables $P_{\Phi,i}$, $P_{\Theta,i}$, $P_{\Psi,i}$, P_S, Φ_i, Θ_i, Ψ_i, S of the extended Hamiltonian system by applying Eqs. (18), (19), and (22) to Eq. (21). They are given by

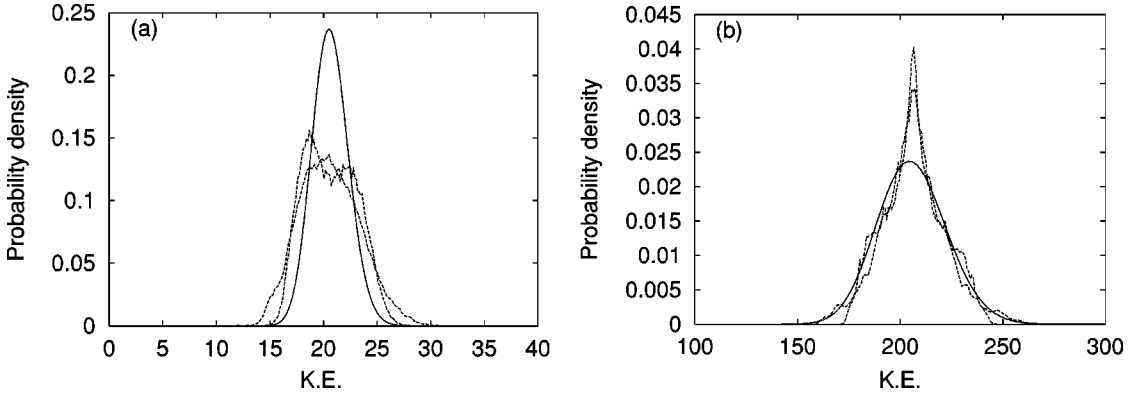

FIG. 2. Comparison of thermostated distributions for the kinetic energy with canonical distributions for two different initial conditions of the 10×10 lattice. The kinetic energy (KE) and the probability density are plotted in the dimensionless units defined in Sec. II. The canonical distributions are shown as solid lines and the two thermostated distributions as dotted lines. (a) $T=20.0$ K and (b) $T=200.0$ K.

$$\frac{dp_{\theta,i}}{dt}=-\frac{\partial V}{\partial\theta_i}-\frac{[p_{\phi,i}-\cos(\theta_i)p_{\psi,i}]p_{\psi,i}}{\sin(\theta_i)}+\frac{[p_{\phi,i}-\cos(\theta_i)p_{\psi_i}]^2\cos(\theta_i)}{\sin^3(\theta_i)}-\frac{p_{\theta,i}P_S}{Q},$$

$$\frac{dp_{\phi,i}}{dt}=-\frac{\partial V}{\partial\phi_i}-\frac{p_{\phi,i}P_S}{Q},\quad \frac{dp_{\psi,i}}{dt}=-\frac{p_{\psi,i}P_S}{Q},$$

$$\frac{dP_S}{dt}=\sum_{i=1}^{N}\left(p_{\theta,i}^2+\frac{[p_{\phi_i}-\cos(\theta_i)p_{\psi,i}]^2}{\sin^2(\theta_i)}+p_{\psi,i}^2\right)-3Nk_BT, \tag{23}$$

$$\frac{d\theta_i}{dt}=p_{\theta,i},\quad \frac{d\phi_i}{dt}=\frac{[p_{\phi,i}-\cos(\theta_i)p_{\psi,i}]}{\sin^2(\theta_i)},$$

$$\frac{d\psi_i}{dt}=p_{\psi,i}-\frac{[p_{\phi,i}-\cos(\theta_i)p_{\psi,i}]\cos(\theta_i)}{\sin^2(\theta_i)},\quad \frac{dS}{dt}=\frac{SP_S}{Q}.$$

These are the dimensionless equations of motion of the thermostated physical system. In subsequent sections, we will take the value of Q to be $Q=1.00$, following the work of Hoover [20] who found the Nosé thermostat to be the most effective at intermediate values of Q in the range of $Q=1.00$.

B. Comparison of thermostated and canonical distributions

We can now determine if the Nosé thermostat thermalizes the lattice of rotors. If thermalization does take place, then we expect that the distribution of energies visited by the thermostated system will agree with the canonical distributions. To calculate the thermostated distributions, we wrote a program implementing the system of equations (23) using an Adams-Gear integration algorithm. In integrating up to a maximum time $t=2000.0$, the energy was recorded at 2×10^4 equal intervals, and the resulting list of energies was sorted into a histogram of 100 bins, which we call the ''thermostated distribution.'' As a check of the integration, we verified that the extended Hamiltonian, Eq. (20), was a constant of motion. Two initial conditions with random positions in the configuration space were chosen for each lattice size. The total kinetic energy of both initial conditions was set to correspond to the temperature of interest; we considered both 20.0 K and 200.0 K.

In order to keep our computer usage manageable, we integrated the thermostated equations for the two total times $t=1000.0$ and $t=2000.0$, with a sampling interval for the energies of $\Delta t=0.1$. We found agreement of the thermostated distributions for $t=1000.0$ and $t=2000.0$, giving an evidence that the distribution has converged to its equilibrium distribution. Since the Lyapounov time $t_L=1/\lambda\approx2.0$ (see Table I), the sampling interval $\Delta t=0.1$ does introduce some correlation into the data. To ensure that this was not a large effect, we took several distributions with total time $t=20\,000.0$ and sampling interval $\Delta t=2.0$, and found very little difference from the distributions with $\Delta t=0.1$.

As mentioned above, because the phase space of the 10×10 lattice is so large, we cannot directly compare the thermostated and canonical distributions for the potential energy, although we can do so for the kinetic energies. Therefore, we first show that the thermostated dynamics gives close agreement for the distribution of the kinetic energies. Then we show that the thermostated 2×2, 4×4, and 6×6 lattices have potential energy distributions that agree well with the expected distributions for the canonical ensemble. We thus expect that the thermostated 10×10 lattice should also agree closely. Finally, we will show (in the following section) that the thermostated average magnetization and energy at low temperature are very close to their expected values for the 10×10 lattice, providing a strong evidence that the agreement extends down to a very low temperature.

In Fig. 2(a), the thermostated distributions of the kinetic energy are compared to the expected thermal distribution of kinetic energies [found from Eqs. (14) and (9)] for two random initial conditions of the 10×10 lattice, at the temperature $T=20.0$ K. Figure 2(b) shows the same comparison at temperature $T=200.0$ K. In both cases, we see small devia-

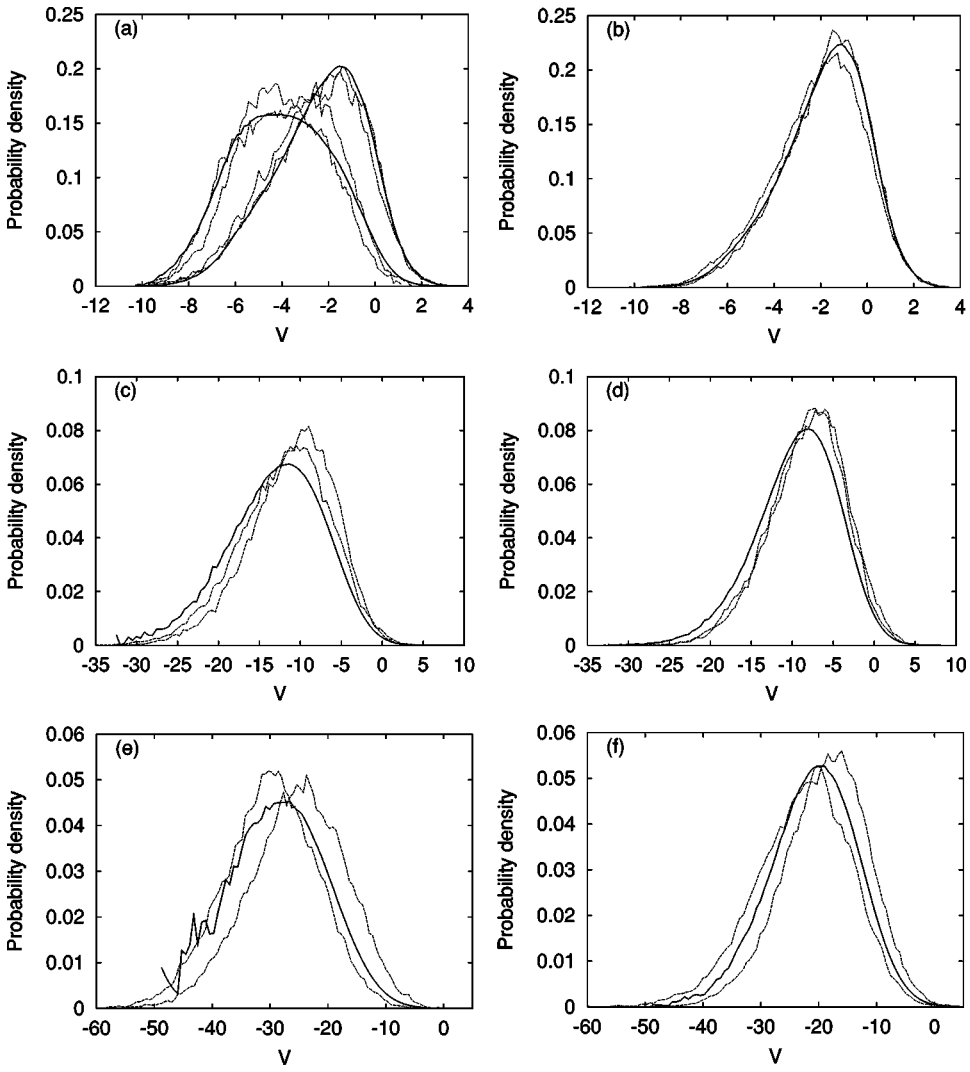

FIG. 3. Comparison of thermostated distributions for potential energy with canonical distributions for two different initial conditions of lattices of increasing size. Both V and the probability density are in the dimensionless units as described in Sec. II. (a) 2×2 lattice at $T=200.0$ K and 400.0 K; (b) 2×2 lattice at 600.0 K; (c),(d) 4×4 lattice at $T=400.0$ K, 600.0 K; and (e),(f) 6×6 lattice at $T=400.0$ K, 600.0 K.

tions in the widths of the distributions (and therefore in the heights, since they are normalized to one), but an overall agreement in the kinetic energy distributions.

Moving to the potential energy distributions, in Fig. 3(a) the thermostated and thermal distributions for a 2×2 lattice at $T=200.0$ and 400.0 K are shown; the distributions for the 2×2 lattice at 600.0 K are presented in Fig. 3(b). The agreement of both initial conditions is quite close at all three temperatures. In Figs. 3(c) and 3(d), a comparison of the distributions for a 4×4 lattice at $T=400.0$ and 600.0 K is shown. (Because of the statistical uncertainties in the density of states, the canonical distribution at $T=200.0$ K was not accurate enough for comparison.) The agreement is quite close for both temperatures, but the thermostated distributions are smaller at lower energies, with a slightly more pronounced effect at $T=400.0$ K. In Figs. 3(e) and 3(f), the comparison is shown for a 6×6 lattice and is very similar to the results for the 4×4 lattice. Based on this trend in the agreement with increasing lattice size, we expect that the 10×10 lattice would give similar results. We will present more evidence for the agreement of the thermostated distributions at lower temperatures in the following section. Thus, we can expect that the thermostated lattice of rotors will be a useful model for a real magnetic material.

IV. CALCULATING THE CRITICAL TEMPERATURE OF THE LATTICE

Before calculating hysteresis loops for the lattice of rotors, we first use the thermostating technique to calculate the heat capacity of the 10×10 lattice, so that we can determine the temperature range where hysteresis loops are expected. In the infinite two-dimensional Ising lattice, the heat capacity

$$C_H=\left(\frac{\partial U}{\partial T}\right)_{H,N} \tag{24}$$

has a logarithmic divergence at the critical point. While in the definition, Eq. (24), the variable U refers to the internal energy, in the case of the Ising lattice U includes only a magnetic potential energy and not a kinetic energy. For our rotor model, the Hamiltonian, Eq. (6), includes both a kinetic and a magnetic potential energy. However, the kinetic energy serves only to allow the Nosé thermostat to produce a canonical distribution [Eq. (10)] of the potential energy at a

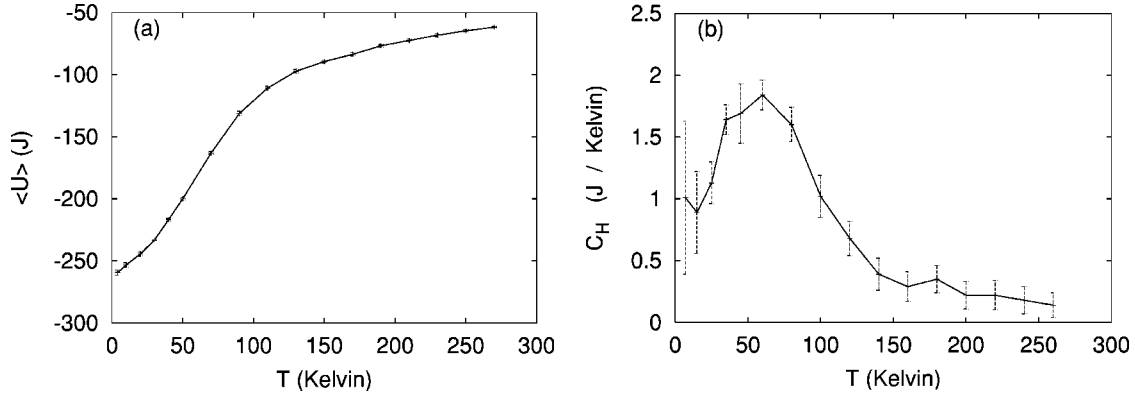

FIG. 4. The thermal average internal energy and the heat capacity of the 10×10 lattice of rotors, calculated using the thermostated equations of motion. The thermal average internal energy (in units of the exchange constant J) is plotted vs temperature in (a). The heat capacity (in units of the exchange constant J/K) is plotted vs temperature in (b). The error bars result from the confidence intervals for the calculated values of the average internal energy.

given temperature. Hence, in finding the heat capacity we include only the magnetic potential energy in the internal energy, and in this section internal energy refers only to this potential energy.

In the 10×10 lattice with Heisenberg exchange, we also expect to see a peak in the heat capacity, defining a transition temperature T_c. (We will verify in more detail that T_c represents the Curie temperature in the following section.) Because of the finite size of the lattice, however, a less sharply defined T_c would be expected, as the magnetic order below T_c cannot have a diverging correlation length. In addition, we expect that the presence of the anisotropy interaction could shift the location of the peak T_c.

To calculate the heat capacity, we started the lattice with initial conditions corresponding to temperatures $T=4.0$, 10.0, 20.0, 30.0, and 40.0 K, and then from $T=50.0$ K to $T=270.0$ K in steps of 20.0 K. The initial conditions were made to correspond to a given temperature by setting the total kinetic energy of the rotors equal to approximately $\frac{3}{2}Nk_BT$. We integrated the thermostated equations of motion for a time $T=500.0$ for 20 different initial conditions at temperatures $T=40.0$ K and above, disregarding the first $t=200.0$ to allow the system to approach equilibrium. We calculated the average internal energy of the lattice for the final $t=300.0$ for each trajectory. From these 20 values for $\langle U\rangle$, we used the t distribution to form a 95% confidence interval [21] for the mean of $\langle U\rangle$ at each temperature. At temperatures below $T=40.0$ K, the lattice could remain in a metastable (i.e., not fully aligned) state for the entire time interval $t=500.0$, with a greater chance of this occurring as the temperature decreased. We can understand this with the observation that below $T=40.0$ K, the relaxation time of the low-energy metastable states becomes comparable to the integration time, and can be much larger than the integration time at the lowest temperature $T=4.0$ K. We thus averaged over 30 initial conditions for temperatures $T=20.0$ and 30.0 K, and over 60 initial conditions for temperatures $T=4.0$ K and $T=10.0$ K in order to sample the thermal distribution more accurately.

We then estimated the heat capacity at temperatures from 7.0 K to 260.0 K (at the midpoints of the intervals defined by the temperatures chosen above) with the linear approximation

$$C_H(T)=\frac{\langle U\rangle|_{T+\Delta T/2}-\langle U\rangle|_{T-\Delta T/2}}{\Delta T}. \tag{25}$$

In Fig. 4(b), we plot the results for the heat capacity, and observe a clear peak at $T_C\approx60.0$ K. At lower temperatures the confidence intervals for C_H, given by

$$\Delta C_H(T)=\frac{\Delta(\langle U\rangle)|_{T+\Delta T/2}+\Delta(\langle U\rangle)|_{T-\Delta T/2}}{\Delta T}, \tag{26}$$

become much larger due to the larger uncertainty in the values of $\langle U\rangle$ [shown in Fig. 4(a)]. Even with the use of more initial conditions, the energies of the low-energy metastable states are given too much weight in the thermostated average at a low temperature, resulting in higher values of $\langle U\rangle$ as well as larger uncertainties.

Still, despite the long relaxation times of the low-energy metastable states, the values for $\langle U\rangle$ do approach the absolute minimum of $E=-267.0$ of the lattice with $\kappa_4=0.67$ and $h=0.0$. An applied field should produce a clear global minimum and decrease the relaxation time of the metastable states, allowing for more accurate thermal averaging. Thus to present further evidence that the thermostated distribution agrees closely with the thermal distribution at low temperatures, we plot in Fig. 5(a) the average internal energy per site $\langle u\rangle=\langle u\rangle/N$ (with 95% confidence intervals) for temperatures $T=20.0$, 10.0, 6.0, and 2.0 K with applied field $h=-1.0$. The minimum of the internal energy per site is $u_{min}=-3.67$, with contributions of -2.00, -0.67, and -1.00 from the exchange, K_4, and magnetic field interactions, respectively. If we extrapolate the linear relationship to $T=0$, we find an intercept of $\langle u\rangle=-3.667$, very close to u_{min}. In Fig. 5(b) we plot for the same temperature range the magnetization per site, $\langle m\rangle=\langle M\rangle/N$, in units of μ, the magnetic moment per site in our dimensionless system of units. We find that $\langle m\rangle$ also increases linearly at low temperature,

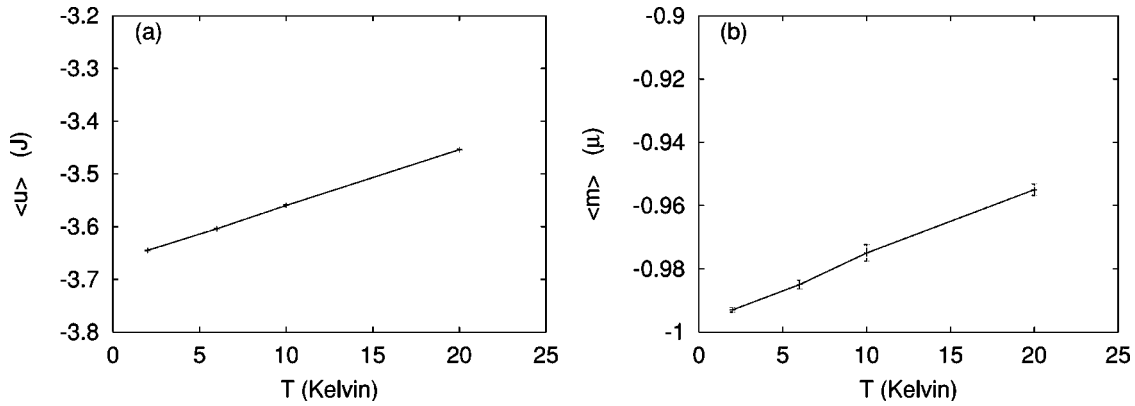

FIG. 5. Thermostated average of (a) internal energy per site $\langle u \rangle$ and (b) magnetization per site $\langle m \rangle$ at low temperature for the 10×10 lattice, with interaction coefficients $\kappa_4 = 0.67$ and $h = -1.00$. Here, $\langle u \rangle$ is in units of the exchange constant J, and $\langle m \rangle$ is in units of the magnetic moment per site μ.

with an extrapolated value at zero temperature of $\langle m \rangle = -0.9974$, quite close to the value $\langle m \rangle = -1.0$ at full saturation.

V. HYSTERESIS IN LATTICE OF ROTORS WITH NOSÉ THERMOSTATING

The Nosé thermostat causes the lattice to move toward an equilibrium distribution and to undergo thermal fluctuations in the equilibrium distribution. In a real magnetic material, when a time-periodic magnetic field is applied, the magnetization lags behind the field because the magnetic moments cannot respond as quickly as the field changes, or because the moments become pinned in a metastable state, for example, when a domain wall becomes stuck at a defect or when a group of spins waits for one spin in the group to nucleate. While our thermostated lattice does not have domain walls or impurities, it is possible for the lattice to become stuck in a metastable state, and also possible for the response of the lattice to lag behind the changing field. Both effects contribute to create hysteresis loops.

In Sec. IV, we found the peak of the heat capacity curve for the 10×10 lattice to be approximately 60.0 K, much lower than the Curie temperature in bulk cobalt of $T_c = 1390$ K. The Curie temperature of a single layer of iron on tungsten [with iron in the crystallographic orientation Fe(110)] is 225 K [22], and as the bulk Curie temperatures of cobalt and iron are comparable (1390 K and 1040 K), this is a good estimate for the Curie temperature of a cobalt thin film as well. With the small planar dimensions of our model further reducing the Curie temperature, a value of 60.0 K for the Curie temperature appears to be reasonable. To ensure that the peak of the heat capacity curve is actually the Curie temperature, we examined the system's approach to equilibrium for initial conditions with randomly oriented spins and several temperatures up to the critical point. The spin orientations at equilibrium shown in Fig. 6 are representative of a sample of several initial conditions at each temperature. In Fig. 6(a), we see that the equilibrium at $T = 10.0$ K consists of spins aligned with one of the minima of the K_4 potential. At $T = 30.0$ K, in Fig. 6(b), we still see the moments aligned along one of the minima of the K_4 interaction, although the higher temperature produces larger fluctuations away from a fully aligned state. In Fig. 6(c) at $T = 50.0$ K, just below the peak temperature of Fig. 4, we see that the correlation length has greatly decreased, supporting the interpretation of the peak of the heat capacity as the Curie temperature. We will look at hysteresis loops in the model at low temperature, in the neighborhood of the Curie temperature, and above the Curie temperature.

As mentioned previously in the description of the thermostated distributions, the equations of motion (23) were integrated using an Adams integration method, with the potential $V(\theta_j, \phi_j, t)$ containing a time-dependent field $h(t) = h_0 \cos(ft)$. To ensure accurate integration of the hysteresis loops, we chose the accuracy of the integration routine to give conservation of H_{ext} from Eq. (20) to seven significant figures in a constant field, and we required that the following condition:

$$\Delta H_{ext} = -\oint M_x(\Theta_j, \Phi_j, t)\, dh, \tag{27}$$

where $M_x(\Theta_j, \Phi_j, t) = \Sigma_{j=1}^{N} \sin(\Theta_j) \sin(\Phi_j)$ was satisfied to five significant figures for each hysteresis loop generated. We used initial conditions with total kinetic energy corresponding to the temperature of the calculation and with randomly oriented moments. In addition, we integrated over four field cycles and averaged over the last three cycles (excluding the first to remove transient behavior) to produce the hysteresis loops. In experiments, the hysteresis loops are typically averaged over a number of field cycles (see Ref. [23], for example). We have averaged over three cycles because of the large amount of computer time needed for the simulation of the lowest frequency, but we find that this is sufficient to give well defined loops.

In Fig. 7, we plot the hysteresis loops for a field strength $h_0 = 3.0$ and for frequencies, $f = 0.001$, 0.005, 0.01, and 0.05. At each frequency, three loops, at temperatures 20.0, 60.0, and 100.0 K, are shown corresponding to the outer, middle, and inner loops, respectively. In Fig. 7(a), the low frequency leads to a steep drop of the magnetization and a square hys-

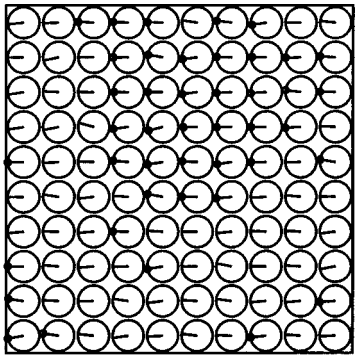

(a)10.0 K

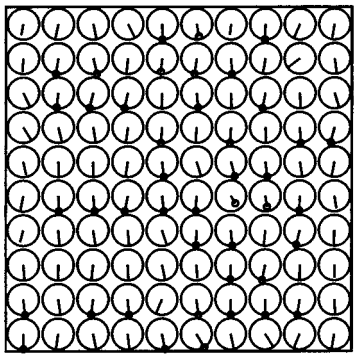

(b)30.0 K

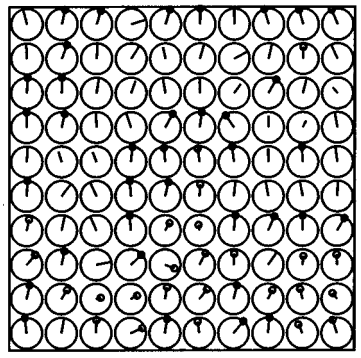

(c)50.0 K

FIG. 6. Spin configurations after movement to equilibrium from a randomly oriented initial state of the 10×10 lattice, at temperatures of 10.0, 30.0, and 50.0 K. The figures show the XY projection of the magnetic moment for each site in the lattice, with a circle at the end of the projection indicating a positive value of S_z for that site.

teresis loop. The coercive field, approximately $h=0.8$ or $\mathcal{H}=hJ/\mu b^2=0.26$ T (using $\mu=1.71\mu_B$ for cobalt) for the $T=20.0$ K loop, decreases for the $T=60.0$ K loops since the lattice, supplied with more thermal energy and now above the blocking temperature, is able to reverse at a lower field strength. At $T=100.0$ K, the lattice is past the blocking temperature and the critical point T_c, but still is caught briefly in a metastable state near zero field. At $T=200.0$ K (not shown), we find that the hysteresis loop disappears, and the magnetization retraces the same path on the return trip of the field.

In Figs. 7(b) and 7(c), the area of the loops at each temperature increases with increasing frequency, as the time for the reversal of the magnetization becomes comparable to the period of the field. We can see that for each temperature, the reversal begins at approximately the same field ($h=-0.8$, -0.3, and $h=0.0$, respectively) but takes a larger and larger portion of the field period as the frequency increases. In Fig. 7(d), the hysteresis loops for $T=60.0$ K and $T=100.0$ K have continued to increase in area; in the hysteresis loop at $T=20.0$ K, however, the magnetization has not finished its reversal before the field reaches its minimum and begins to increase, leading to an oval shape differing from the more familiar S-shape taken by the rest of the loops.

Although our model applies most directly to a nanoparticle with monolayer thickness, we can make an approximate comparison to an experiment performed by Wernsdorfer *et al.* [6]. In the experiment, elliptic nanoparticles were defined from sputtered thin films of Ni, Co, and other materials; the particles had thicknesses between 8 and 50 nm, and had elliptic axis lengths between 50 nm and 1 μm. A small superconducting quantum interference device (SQUID) was deposited next to the particles, and detected the flux change due to the changing magnetization of the particle. Since the field was applied in the plane of the particle and the SQUID, it did not affect the measurement of the flux.

We can compare the hysteresis loops from our model to the hysteresis loop pictured in Fig. 3 of Ref. [6] for the Co particle with dimensions of either 200×100 nm or 100×50 nm, and thickness in the range from 8 nm to 30 nm. In [6], Wernsdorfer *et al.* show that the distribution of switching fields agrees with the prediction of the Néel-Brown model (which assumes a single domain) up to 6 K, so we can reasonably neglect the dipole-dipole interaction in our model. Also, as mentioned above, since the exchange length in cobalt is about 7.0 nm [7] and the lattice spacing is 0.355 nm [8], the spin orientation in the nanoparticle can be considered constant over ~20 atoms. We can therefore expect that the lattice of blocked spins forms a single domain and will apply approximately to the Co nanoparticle.

We note that the shape of the hysteresis loop at 20.0 K and $f=0.001$ in Fig. 7(a) closely resembles the shape of the hysteresis loop for the cobalt nanoparticle, with slightly more rounding due to the higher temperature of Fig. 7(a). The coercive field found for the cobalt nanoparticle in Ref. [6] is $60kA/m=0.07$ T, while the coercive field for our model at 20.0 K at the lowest frequency is 0.26 T. Given the monolayer thickness of our model, this order of magnitude difference is not unexpected. Several factors, however, suggest that the model can be made more accurate. The first is that we have used a value for the four-way anisotropy of cobalt, $\kappa_4=0.67$, appropriate for a surface, but it is known that the value of the anisotropy in the bulk is lower [24]. Using values of $\kappa_4=0.2$ and 0.1, we found coercive fields $H_c=0.09$ and 0.07 T, respectively. Choosing these values for κ_4 would make our model an effective two-dimensional model, with a parameter borrowed from the bulk. The second factor is that, while we have used periodic boundary conditions in an effort

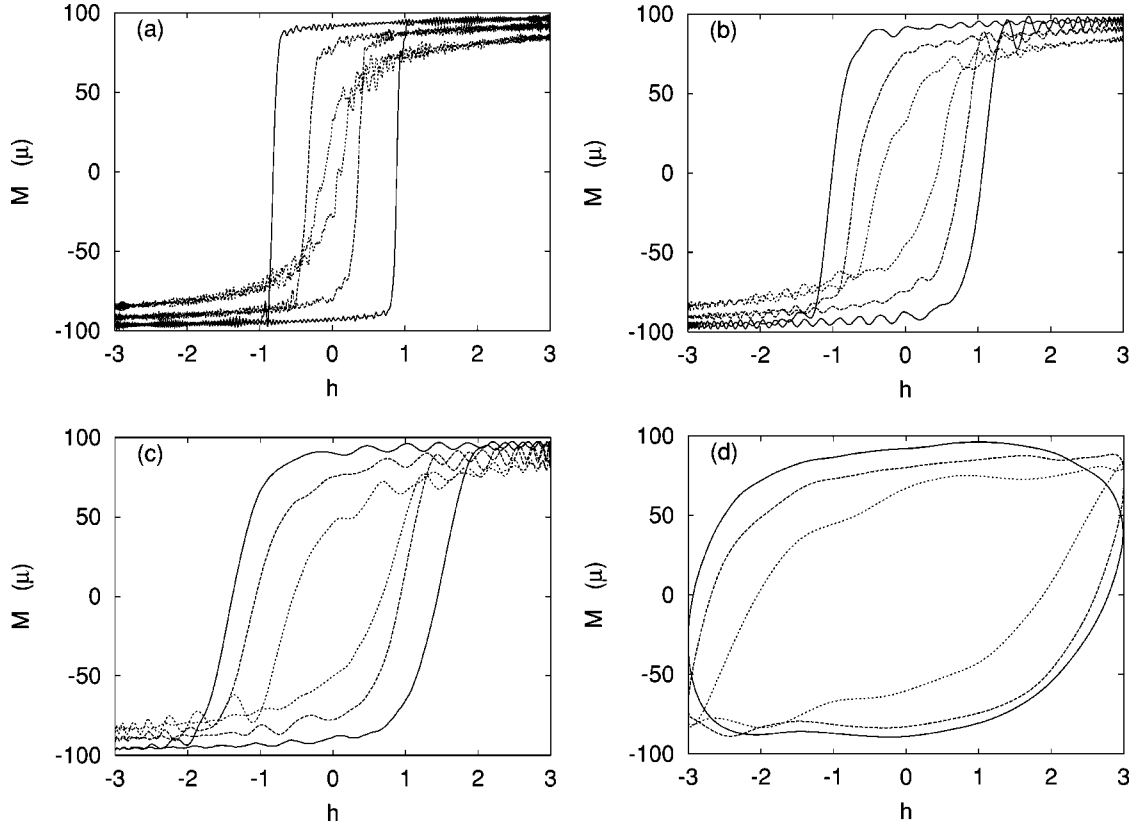

FIG. 7. Plots of M (averaged over three field cycles) vs h for frequencies (a) $f=0.001$, (b) $f=0.005$, (c) $f=0.01$, and (d) $f=0.05$. Each plot shows three hysteresis loops at $T=20.0$, 60.0, and 100.0 K, progressing from the outer to inner loop with increasing temperature. M is plotted here in units of the magnetic moment per site μ, and h is in the dimensionless units described in Sec. II.

to increase the effective size of our model, changing the boundary conditions from periodic to nonperiodic is probably more realistic for a nanoparticle. This reduces the coercive field by 5%, with nucleation beginning at the corners of the square lattice where the sites have a lower coordination number of 2. Modeling the elliptical shape of the nanoparticle would create a number of edge atoms with coordination number 2, and would likely reduce the coercive field further.

VI. THE APPROACH TO EQUILIBRIUM

Since the lattice model does not have an intrinsic time scale (as described in Sec. II, this allows the model to be applied to different physical systems), we need to make a correspondence between the dynamics of the Co nanoparticle and the lattice. We can use data for the approach to equilibrium (magnetization reversal) in the experiment to set the time scale for the lattice model.

In their paper, Wernsdorfer *et al.* [6] apply the Néel-Brown theory [25,26] of activation over a single energy barrier to analyze their data for the distribution of the switching field, and are able to find a close fit to their experimental data. According to the Néel-Brown theory, which applies to a single-domain particle, the energy barrier E to reversal in a given field H is found to be

$$E(H)=E_0\left(1-\frac{H}{H_{SW}^0}\right)^{\alpha}, \tag{28}$$

where E_0 and H_{SW}^0 are the energy barrier and reversal field at zero temperature, and α is found to be 1.5. At a finite temperature, the survival probability for the magnetization (the probability not to have switched) after a time t is given by the exponential $P_{sur}(t)=e^{-t/\tau}$, where

$$\tau(T,H)=\tau_0\,\exp\left(\frac{E(H)}{k_BT}\right). \tag{29}$$

In their analysis of the switching field, Wernsdorfer *et al.* find an estimate for the prefactor τ_0 of 7.4×10^{-7} s; it is also possible to estimate τ_0 directly from the survival probability $P_{sur}(t)$, and we will do that here for the lattice of rotors to establish a time scale for our model.

The first step in obtaining the survival probability is to find the histogram of switching times. As outlined in Ref. [27], we placed the rotor lattice in an opposed field $h=-0.75$ close to the switching field for 200 initial conditions near saturation (each of the trajectories initially has magnetization near saturation, M_s). We then plotted a histogram (normalizing its area to one) of the times taken for the magnetization to reverse, where reversal was defined as the first time when the magnetization reached $-0.85M_s$. (Note that the exact value of this cutoff is arbitrary, and the cutoff needs only to fall close to the saturation value M_s.) Integrating the histogram from time $t=0$ to time t gave the probability $P_{sw}(t)$ of the magnetization having switched by time t, and finally we calculated $P_{sur}(t)=1-P_{sw}(t)$.

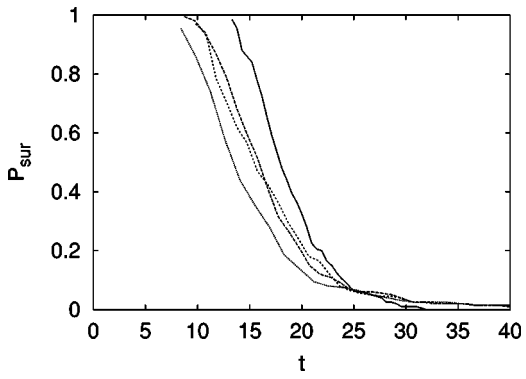

FIG. 8. Survival probability P_{sur} vs t for the 10×10 lattice of rotors initially aligned and placed in a reversal field of $h=-0.75$. Here, P_{sur} is unitless, and the time t is plotted in the dimensionless units defined in Sec. II. The data are shown for four different temperatures $T=40.0$, 30.0, 20.0, and 10.0 K, with the distribution at 10.0 K at longest times and the times decreasing with increasing temperature. The distributions are based on 200 measurements of magnetization reversal at each temperature.

The results for temperatures 10.0, 20.0, 30.0, and 40.0 K are shown in Fig. 8. The distributions do shift to greater times as the temperature decreases, and after a certain delay time follow an exponential form, as predicted by Eq. (29). We think the delay time is due to the fact that the thermostated equations retain the original spin dynamics of the unthermostated system, as well as thermal relaxation, while the Néel-Brown model applies to a system undergoing only the thermal relaxation.

If we use the time that the switching time distributions takes to decrease to $1/e$ as a value of τ for each temperature, and perform a best fit for the quantity τ_0, we find $\tau_0 \approx 14.4$. We can make a rough correspondence between this time and the time $\tau_0=7.4\times10^{-7}$ s in the experiment, to find the time unit $\sqrt{I/J}=5.1\times10^{-6}$ s. This also establishes the unit of frequency in our model as 2.0×10^5 Hz, giving for the frequency range used in the hysteresis loops in Fig. 7 a range from 2.0×10^2 to 1.0×10^4 Hz. From the value of the time unit we can also find the effective moment of inertia of the rotors to be $I=5.2\times10^{-32}$ kg m^2. (Since the moment of inertia does not correspond directly to the atoms in the material but allows coupling of the magnetic degree of freedom to the thermal degrees of freedom, we do not expect to be able to relate I to the size or mass of the atoms.)

VII. CONCLUSIONS

We have studied the appearance of hysteresis in the response of a thermostated 10×10 lattice of magnetic rotors to a time-periodic magnetic field at low temperature. The equations of motion were placed in dimensionless units for the integration; the values of the exchange J and the rotor moment of inertia I, which together give a physical meaning to the dimensionless quantities, were determined by the system being modeled. The hysteresis seen is a consequence of the metastable states created by the surface anisotropy and the exchange interaction, and is made possible by the thermalization introduced by the Nosé thermostat. The underlying chaotic dynamics of the rotor lattice is essential to the thermalization by the Nosé technique.

For the values of J and K_4 we used, the lattice was determined to have a Curie temperature of $T_c\approx60.0$ K. Given that the 10×10 lattice has both the small dimensions of a nanoparticle and the thickness of a thin film, this value is reasonable. In comparison of hysteresis in the lattice to the hysteresis observed by Wernsdorfer *et al.* [6] in a cobalt nanoparticle, the experimental coercive field was 0.07 T and our model gave a value of 0.26 T. The reduced value of K_4 in the bulk and the use of nonperiodic boundary conditions both indicate a potential for improved agreement. A comparison with experimental data for the switching time distribution sets the time (and frequency) scale for our model as applied to the cobalt nanoparticle, and allowed a determination of the effective moment of inertia I of the rotors in the lattice model.

As our available computing power is increased, we are working to extend the model to a three-dimensional lattice. We think this can improve the agreement with experiment by lowering the κ_4 anisotropy used, thus decreasing the coercive field, and by increasing the average coordination number, which should increase the critical temperature.

ACKNOWLEDGMENTS

The authors wish to thank the Robert A. Welch Foundation, Grant No. F-1051, and the Engineering Research Program of the Office of Basic Energy Sciences at the U.S. Department of Energy, Grant No. DE-FG03-94ER14405, for partial support of this work. We also thank the University of Texas High Performance Computing Center for use of its facilities.

[1] W. Lo and R. Pelcovits, Phys. Rev. A **42**, 7471 (1990).
[2] M. Acharyya and B. Chakrabarti, Phys. Rev. B **52**, 6550 (1995).
[3] F. Zhong, J. Zhang, and G. Siu, J. Phys.: Condens. Matter **6**, 7785 (1994).
[4] D. Rapaport and D. Landau, Phys. Rev. E **53**, 4696 (1996).
[5] A. Moschel, R.A. Hyman, A. Zangwill, and M. Stiles, Phys. Rev. Lett. **77**, 3653 (1996).
[6] W. Wernsdorfer, K. Hasselbach, D. Mailly, B. Barbara, A. Benoit, L. Thomas, and G. Suran, J. Magn. Magn. Mater. **145**, 33 (1995).
[7] M. Schabes, J. Magn. Magn. Mater. **95**, 249 (1991).
[8] *CRC Handbook of Chemistry and Physics: Student Edition*, edited by D.R. Lide (CRC Press, Boca Raton, 1993).
[9] M. Bander and D. Mills, Phys. Rev. B **38**, 12 015 (1988).
[10] H. Goldstein, *Classical Mechanics* (Addison-Wesley, Reading, MA, 1980), pp. 143–148.
[11] D. Craik and R. Tebble, *Ferromagnetism and Ferromagnetic*

Domains (North-Holland, Amsterdam, 1965).
[12] B.H.M. Kowalewski, C.M. Schneider, and B. Heinrich, Phys. Rev. B **47**, 8748 (1993).
[13] E. Wohlfarth, *Ferromagnetic Materials: A Handbook on the Properties on Magnetically Ordered Substances* (North-Holland, Amsterdam, 1980).
[14] H.A. Posch, W.G. Hoover, and F.J. Vesely, Phys. Rev. A **33**, 4253 (1986).
[15] G. Benettin, L. Galgani, and J.-M. Strelcyn, Phys. Rev. A **14**, 2338 (1976).
[16] L. Reichl, *The Transition to Chaos in Conservative Classical Systems: Quantum Manifestations* (Springer-Verlag, Berlin, 1992).
[17] K. Huang, *Statistical Mechanics* (Wiley, New York, 1987), pp. 138 and 139; L. E. Reichl, *A Modern Course in Statistical Physics* (Wiley, New York, 1998).
[18] S. Nosé, Mol. Phys. **52**, 255 (1984).
[19] S. Nosé, J. Chem. Phys. **81**, 511 (1984).
[20] W.G. Hoover, Phys. Rev. A **31**, 1695 (1985).
[21] R.V. Hogg and A.T. Craig, *Introduction to Mathematical Statistics* (Prentice-Hall, Englewood Cliffs, NJ, 1995), pp. 214–217, 268–274.
[22] P. Grunberg, J. Phys.: Condens. Matter **13**, 7691 (2001).
[23] Y.-L. He and G. Wang, Phys. Rev. Lett. **70**, 2336 (1993).
[24] M. Respaud *et al.*, Phys. Rev. B **57**, 2925 (1998).
[25] L. Néel, Ann. Geophys. **5**, 99 (1949).
[26] W.F. Brown, Phys. Rev. **130**, 1677 (1963).
[27] W. Wernsdorfer, E. Orozco, K. Hasselbach, A. Benoit, B. Barbara, N. Demoncy, A. Loiseau, H. Pascard, and D. Mailly, Phys. Rev. Lett. **78**, 1791 (1997).